Representative linearised models for a wave energy converter using various levels of force excitation

Mahdiyeh Farajvand [a,*], Demián García-Violini [a,b,c], John V. Ringwood [a]

[a] *Centre for Ocean Energy Research, Maynooth University, Maynooth, Co. Kildare, Ireland*
[b] *Departamento de Ciencia y Tecnología, Universidad Nacional de Quilmes, Roque Saenz Peña 352, Bernal B1876, Argentina*
[c] *Consejo Nacional de Investigaciones Científicas y Técnicas (CONICET), Argentina*

ABSTRACT

In guiding the progression, development, and operation of wave energy converters (WECs) in a more efficient way, mathematical analysis and understanding of the dynamic process is essential. Mathematical WEC models, obtained either by numerical analysis or physical modelling, form the basis of most (model-based) energy maximising control strategies available in the literature, where experimental design and system identification methodology directly impact the resulting model. This study, using an experimental-based WEC model (which can be used for linear control design), investigates the dynamic behaviour of a WEC by analysing the dominant poles of the system, generated using fully nonlinear computational fluid dynamics (CFD)-based numerical wave tank (NWT) experiments. The aim is to effectively track the dominant dynamics of the WEC, using different force-input amplitude levels in the NWT setup, and perform a comparison with the classical linear boundary-element-methods (BEM) equivalent methodology. Thus, the presented case studies are shown to agree with previously proposed model assessment of linear WEC models, based on a free-decay NWT setup. In addition, the representative WEC models determined as part of this study can be used for WEC controller design, either singly, or using a form of model/controller gain scheduling.

1. Introduction

Considerable modelling and testing is required for the development, optimisation, and power production assessment of wave energy converters (WECs). It is essential to accurately model WECs, and to measure, estimate, and monitor their dynamics in order to design effective (model-based) energy maximising control strategies, while preventing device damage due to undamped oscillations, or excursions beyond physical constraints, during operation. Developing a representative WEC model to describe body motion, wave–structure interaction, and the dynamics of different energy conversion stages is fundamental. Commonly used WEC models for control strategies are typically based on linear hydrodynamic models, either obtained from linear potential flow theory or data-driven system identification methodologies. Linear WEC models, based on boundary element methods (BEM), result in computationally attractive models commonly used for model-based control strategies, where the frequency-dependent hydrodynamic parameters are obtained under the assumption of inviscid, irrotational, and incompressible flow and *small body motion* (relative to the body dimension) around the equilibrium point. However, linear models, developed under these assumptions, and small wave amplitude/steepness,

are in conflict with the requirement of exaggerated device oscillations, as a consequence of the optimal energy-maximisation conditions (Windt et al., 2021). In contrast, nonlinear approaches for mathematical modelling of WECs, reviewed in Penalba et al. (2017), point to techniques which can capture nonlinear hydrodynamic (and other) effects, and/or provide high fidelity data. Nonlinear WEC hydrodynamic effects can be handled using different strategies, namely, *partially* nonlinear methods, based on expansion of the linear model by including some nonlinear effects (Merigaud et al., 2012), *weakly* nonlinear methods, based on simplification of the fully nonlinear formulation (Letournel et al., 2014), and *fully* nonlinear models (Babarit et al., 2009). Among modelling techniques in the field of WECs, computational fluid dynamics (CFD)-based analysis, capable of fully capturing hydrodynamic nonlinearities (consistent with the Navier–Stokes equations), is useful for high-fidelity modelling of WECs, but at great computational expense (Windt et al., 2019). Nevertheless, CFD-based numerical wave tank (NWT) models have shown to be powerful tools, providing high-fidelity time-domain analysis of WECs, and power production assessment (Windt et al., 2018, 2020).

In order to produce computationally simpler models, while considering WEC nonlinearity, recent efforts have aimed at the development

---

of representative linear models, using system identification methodologies, from nonlinear NWT experiments, where the design of the NWT testing setup for data generation, and the employed system identification techniques, impact the resulting identified WEC model. This can be viewed as a data-based form of model reduction. For instance, Farajvand et al. (2021) developed a framework to identify a nominal linear model for application of a robust control strategy from force-input CFD-based NWT (CNWT) experiments, following an empirical transfer function estimate (ETFE) methodology, essentially using a black-box identification method. Similarly, Armesto et al. (2014) proposed a solution for parameter identification of a state-space WEC representation from a series of (zero-input) decay tests in a CNWT setup. The study in Davidson et al. (2015) uses a linear modelling approach for WECs, combining high-fidelity CNWT simulations, system identification, and BEM-based modelling methods.

There is motivation to apply system identification strategies to wave energy modelling to characterise the movement of the WECs. The study in Bacelli et al. (2017) considers system identification techniques and model validation procedures to calculate the WEC dynamics based on data from wave tank experiments. The FOAMM toolbox (Pena-Sanchez et al., 2019) provides an identification technique capable of computing parametric WEC models, which can characterise the system dynamics. This toolbox systematically implements a moment-matching (Faedo et al., 2018) based identification strategy from nonparametric frequency-domain data.

The novelty of the present study is to model the state-space form of a WEC system and investigate the *dominant* dynamics, particularly considering *force-input* experiments in the CNWT setup. The FOAMM toolbox is used to implement the frequency-domain identification through the moments (key frequencies) of the ETFEs calculated from input/output data. Compared to similar studies in the literature, which use system identification based *free-decay* experiments in a CNWT setup (Davidson et al., 2015), and basically focus only on parameters connected with inertia, restoring, and damping forces, the current study with appropriate selection of input force levels, covering the main range of frequencies and amplitudes of the device, is capable of determining a sufficiently representative model of the total system dynamics. Furthermore, as the force inputs acting on the WEC system for the system identification process are basically applied through the power take-off (PTO) system, the identified linear models can be used for linear model-based WEC control design. A comparison of the dominant dynamics from the force-input experiments with a BEM-based linear model is also performed, as a baseline. The overview of the sequences of steps to perform the dominant dynamics assessment from CNWT and WAMIT setups is outlined in Fig. 1.

The NWT considered for the experiments is a modified version of the setup presented in Farajvand et al. (2021) for system identification tests. Sinusoidal input signals, covering the most significant frequency range of the device and full input and output signal ranges, are used to provide the data for the system identification process.

Using different levels of input amplitude forces, WEC models are identified at each amplitude level and the dominant dynamics of the system, most notably the resonance frequency and pole location trends, have been tracked. Finally, a comparison of the dynamical behaviour of the system obtained with the presented study, using *force-input* NWT experiments, with equivalent *free-decay* NWT experiments as presented in Davidson et al. (2015), have been drawn.

The remainder of the paper is laid out as follows. Initially, standard linear modelling assumptions, as well as essential properties of WEC systems, are recalled in Section 2. The NWT specifications, used as the experimental setup, are provided in Section 3. Next, the experiment type, i.e. force-to-velocity experiments, used to obtain data for the system identification procedure, is detailed in Section 4. The system identification methodology applied to the generated data is presented in Section 5. The case study, including NWT features, the input force signals, and the results of the system identification and dominant pole analysis, follows in Section 6 and, finally, overall conclusions from the study are drawn in Section 7.
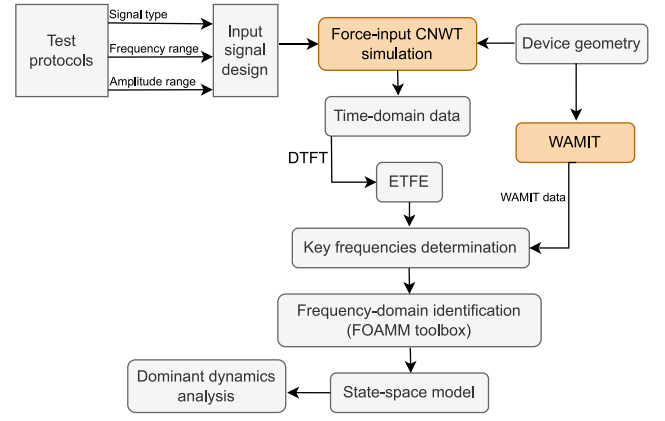

Fig. 1. Overview of the sequences of steps to perform dominant dynamic assessment from CNWT and WAMIT setups.

2. Linear models for wave energy systems

Mathematical WEC models, under the assumption of linearity, are commonly studied using linear potential flow theory and the well-known Cummins' equation (Cummins, 1962), where the motion of a single degree of freedom (DoF) floating structure, in the time domain, can be expressed as:

$$(m + m_\infty)\ddot{y}(t) = f_{ex}(t) - f_u(t) - k_h y(t) - h_r \star \dot{y}(t), \quad (1)$$

where $y(t)$, $\dot{y}(t)$, and $\ddot{y}(t)$ are the device displacement, velocity, and acceleration, respectively, with '$\star$' representing convolution. $f_{ex}(t)$ is the wave excitation force, produced by the action of incoming waves, $f_r(t)$ is the radiation force, arising from device motion in the fluid ($h_r(t)$ the radiation impulse response function), $f_u(t)$ is the control input applied by means of the PTO system, and k_h the hydrostatic stiffness, related to buoyancy/gravity forces. $m \in \mathbb{R}^+$ is the mass of the device and $m_\infty = \lim_{\omega \to +\infty} A_r(\omega)$ the added mass at infinite frequency, where $A_r(\omega)$ and $B_r(\omega)$ are the so-called radiation added-mass and damping, respectively, defined from Ogilvie's relations (Ogilvie, 1964) as:

$$A_r(\omega) = m_\infty - \frac{1}{\omega} \int_0^{+\infty} h_r(t) \sin(\omega t) dt,$$
$$B_r(\omega) = \int_0^{+\infty} h_r(t) \cos(\omega t) dt. \quad (2)$$

Eq. (2) fully characterises the Fourier transform of $h_r(t)$, i.e.

$$H_r(\omega) = B_r(\omega) + J\omega \left[A_r(\omega) - m_\infty \right], \quad (3)$$

where $h_r(t)$ and $H_r(\omega)$ denote a Fourier transform pair. Using Eq. (3), the model in Eq. (1) can be compactly expressed (Falnes, 2002), in the frequency domain, as follows:

$$V(\omega) = \frac{1}{Z_i(\omega)} \left[F_{ex}(\omega) - F_u(\omega) \right], \quad (4)$$

where

$$Z_i(\omega) = B_r(\omega) + J\omega \left(m + A_r(\omega) - \frac{k_h}{\omega^2} \right). \quad (5)$$

Considering the force-to-velocity mapping in the Laplace domain (García-Violini et al., 2020):

$$G(s) = \frac{s}{s^2(m + m_\infty) + s\hat{H}_r(s) + k_h} \bigg|_{s=J\omega} \approx \frac{1}{Z_i(\omega)}, \quad (6)$$

where $H_r(\omega)$ is commonly computed using boundary-element methods, such as WAMIT (Wamit Inc, 2022), and $\hat{H}_r(s) \approx H_r(\omega)$, for $s = J\omega$, with $\hat{H}_r(s)$ a stable linear time-invariant (LTI) system.

Cummins' equation can be implemented numerically directly by numerical convolution, or by first approximating the convolution term in state-space sub-system form and then calculating the state-space

representation of Eq. (1), according to the study in (Davidson et al., 2015):

$$\dot{x}(t) = Ax(t) + Bu(t), \quad y(t) = Cx(t) + Du(t), \tag{7}$$

In Eq. (7), $x(t)$ is the state vector and the function $u(t)$, defined as $u(t) = f_{ex}(t) - f_u(t)$, is the input of the system. A, B, C, and D are the state (dynamic), input, output, and direct transmission matrices, respectively. Matrix D is a null matrix (zero matrix), as $G(j\omega)$ in Eq. (6) is strictly proper (for real (physical) WEC systems the matrix D is the null matrix).

2.1. WEC systems essential properties

After defining the WEC model, it is crucial to consider the fundamental properties which are key drivers for dynamic system analysis and synthesis. Fundamentally, WECs are characterised by the properties of stability and passivity (Pérez and Fossen, 2008).

2.1.1. Stability

Maintaining the stability of WEC structures exposed to external loading with different frequencies and amplitudes is one of the main priorities. Stability analysis of WECs has been carried out using different strategies. Perez and Fossen (2011) stabilises unstable identified models by means of reflecting the unstable poles in the imaginary axis (reflecting from the right-hand side to the left-hand side of the complex plane) and reconstructing the model. Another methodology for guarantying stability is proposed in Davidson et al. (2015) by applying constraints on the model parameters.

2.1.2. Passivity

Passivity (related to stability of systems), is a particular case of 'dissipativity', arising from an intuitive interpretation of system behaviour. The concept is formalised based on the physical energy process of the system, assuming that any increase in the system energy is purely from external sources. Passivity for LTI systems can be guaranteed with the phase range saturated to ±90° degrees *for the complete spectral domain*, based on Bode plot shaping, or with a positive real transfer function for all frequencies (Khalil, 2014; Pérez and Fossen, 2008);

$$G(j\omega) + G^H(j\omega) > 0, \ \forall \omega \in \mathbb{R}, \tag{8}$$

where the symbol H denotes the self-adjoint matrix (Hermitian), and equivalently for SISO systems:

$$\mathbb{Re}\,(G(j\omega)) > 0, \ \forall \omega \in \mathbb{R}, \tag{9}$$

so the entire Nyquist plot lies in the right-half plane. Then, the transfer function is given, using the state-space representation in Eq. (7), as follows:

$$G(s) = C\,(sI - A)^{-1}\,B + D, \tag{10}$$

while the passivity of the system (Eqs. (7) and (10)) is guaranteed with a passive sub-state space representation for the radiation structure, in Eqs. (2) and (3) (Pérez and Fossen, 2008). A recent practical passivisation methodology, considering the passivity of nominal linear and uncertainty models for a WEC, is proposed by García-Violini et al. (2021) for the application of a robust spectral-based control methodology.

3. Numerical wave tank

The three-dimensional NWT setup considered for this study uses a point absorber-type WEC. To simplify the NWT illustration, analysis, and identification test, the WEC structure consists of a single degree of freedom, only oscillating in heave, which also eliminates potential effects of motion coupling. For the specific application of system identification tests, the tank is designed with equal spans in the x
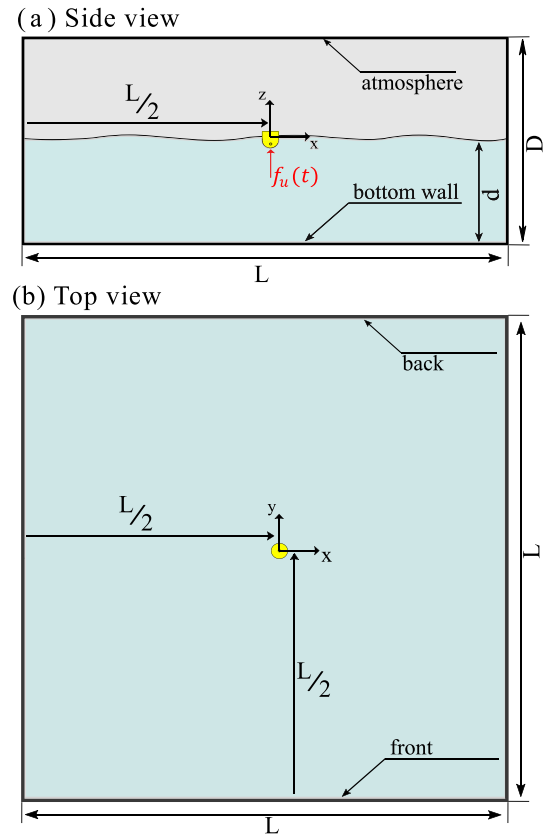

Fig. 2. Schematic of the numerical wave tank for (a) Side view (b) Top view.

and y-directions (perpendicular to the tank depth, in the z-direction), and the buoy is located in the centre of the tank corresponding to $(x, y, z) = (0, 0, 0)$. To avoid reflections of the WEC-induced waves, the tank is equipped with wave absorbers, at the left and right boundaries ($x = \pm L/2$), consistent with the operation of the NWT in a wave flume mode (Windt et al., 2021). The tests are performed by applying a defined external input force ($f_u(t)$) directly to the WEC to induce WEC motion. The side view and top view of the NWT are shown in Fig. 2(a) and (b), respectively, where L is the tank length in x- and y-directions, D and d are the tank, and water, depths, respectively. The tank length is designed to be six wavelengths of the most significant radiated waves (occurring at peak frequency of the radiation damping of the WEC), under the assumption of deep-water conditions. The symmetry configuration of NWT in both the x- and y-directions allows the CFD simulation to be carried out on a *quarter of the full NWT*, with a significant reduction in computation time. NWT mesh generation uses the *blockMesh* utility supplied with OpenFOAM, with finer meshes around the WEC boundary, gradually getting coarser towards the NWT boundary. NWT simulation is implemented using the mesh-based CFD method via numerical solution of the Navier–Stokes (NS) equations (Farajvand et al., 2021) in OpenFOAM.

4. Force-to-velocity experiments

In this study, the input/output data, for system identification and dynamical assessment of the WEC structure, are taken from the CNWT, with the buoy motion resulting from a defined external input (PTO) force, applied directly to the WEC. Due to the nonlinear nature of the fluid/structure interaction, the input force is designed in a way to cover the complete range of frequencies and amplitudes corresponding to typical scaled (Froude scaling with a scaling factor of 1/30th, emulating the full-scale conditions at the AMETS test site in Bellmullet, Co. Mayo,

off the West Coast of Ireland Heller (2011)) operational conditions, in order to obtain a complete hydrodynamic representation of the system. Consequently, exciting the system by applying the input force (PTO force), $f_u(t)$, generates a corresponding output (velocity), $v(t)$, in the time domain, both of which are used to identify the so-called *force-to-velocity* mapping. In this study, a frequency-domain representation, from the time-domain input/output data of the NWT simulations, is obtained through calculation of the discrete-time Fourier transform (DTFT) of input and output signals, at the frequencies at which the spectral analysis is required.

5. System identification method

The objective of system identification is to model the system from the measured input/output signals. The identification procedure can produce either parametric or non-parametric models where, in the parametric case, the dynamic behaviour of the system is described by partial, or ordinary, differential equations. In the non-parametric case, the system response is obtained directly, or indirectly, from experimental data, in time- (impulse response) or frequency-domain (frequency response). A frequency-domain empirical transfer function estimate (ETFE), representing the system frequency response, offers a non-parametric representation of the system dynamics, computed by dividing the DTFT of the output with $F_u(\omega)$, the known DTFT of the input, as:

$$\text{ETFE}(\omega) = \frac{\text{DTFT}(v[n])}{F_u(\omega)} \quad (11)$$

Note that, in Eq. (11), the discrete-time Fourier transform is employed, since the (sinusoidal) frequency is known, with just the amplitude and phase to be determined. Furthermore, the DTFT of the input signal, $F_u(\omega)$, is trivial (user defined sinusoidal input signal with known amplitude and phase), so these parameters are substituted directly.

The DTFT calculates a frequency-domain representation of a signal at a single frequency point. The DTFT of a sequence of N equispaced samples of a finite discrete-time series signal $v[n]$[1] ($v[n] = v(nT_s)$ where T_s is sampling period), considering a sequence of N samples, where $0 \le n \le N-1$, is depicted as $V(e^{j\omega})$ with ω being the real frequency variable ($0 \le \omega \le 2\pi$), defined as

$$V(e^{j\omega}) = \sum_{n=0}^{N-1} v[n]w[n]e^{-j\omega n}, \quad (12)$$

where $w[n]$ is a window function. Note that, in calculating a short-term Fourier transform, it is customary to employ a non-rectangular window function to reduce the effect of spectral leakage, caused by the abrupt start and finish of the data record. The choice of window function is discussed further in Section 5.1.

Regarding parametric models, a useful classification (Ljung, 2010), considering the connection of the model to physical (parametric) quantities, is:

- White-box, where all the parameters of the physical system are estimated from the data,
- Grey-box (and the sub-classes of off-white, smoke-grey, steel-grey and slate-grey), where the generic model structure has some connection to the physical model at various levels, and
- Black-box, where the model structure, capable of reproducing the experimental output data, excited with the same input, cannot be physically interpreted, which means that its states have no connection to the physical world.

In general, no hydrodynamic models are truly white-box, in that there is no direct relationship between the physical system parameters and the hydrodynamic 'coefficients', which are usually provided in non-parametric frequency-, or time-domain, as in (5). However, hydrodynamicists may be more comfortable with the individual determination of the non-parametric hydrodynamic quantities corresponding to added mass (A_r) and radiation damping (B_r). For a system identified purely from data, the models are usually limited to black- or, at best, grey-box, where some information about the likely order of the model can be used to specify the structure of the parametric model.

5.1. Window function

A non-rectangular window function is used both to alleviate the effect of spectral leakage due to abrupt termination of the short-term data segment (at both ends), while also minimising the effect of the leading transient in the output signal. A well-known window function, used in conjunction with a short-term Fourier transform, is the Tukey window (tapered cosine window) which is generated by convolving a cosine lobe with a rectangular window. The time-domain representation of the Tukey window (Prabhu, 2014) is:

$$w[n] = \begin{cases} 1, & 0 \le |n| \le (1-\alpha)\frac{N}{2} \\ 0.5\left[1 + \cos\left(\frac{\pi(n-(1-\alpha)\frac{N}{2})}{\alpha\frac{N}{2}}\right)\right], & (1-\alpha)\frac{N}{2} \le |n| \le \frac{N}{2} \end{cases} \quad (13)$$

where α ($0 \le \alpha \le 1$) is a parameter controlling the gradual change between a rectangular window ($\alpha = 0$) and a Hanning window ($\alpha = 1$). The application of the Tukey windowing directly affects the magnitude of the signal in the spectral domain. To compensate for the amplitude distortion due to windowing, an amplitude correction factor is applied, based on a gain calculation by dividing the amplitude of the *known* sinusoidal input signal by magnitude of the Tukey-windowed sinusoidal signal in spectral domain.

5.2. Moment-based system identification

A particular, frequency-domain, system identification strategy, specifically oriented to WEC modelling, is the FOAMM (Pena-Sanchez et al., 2019) MATLAB toolbox, which identifies a parametric model (in state-space form) for WEC dynamics, based on a moment-matching approach. A notable feature is the ability to pre-specify particular key frequency points at which exact matching between the parametric model and the non-parametric ETFE is achieved, which can include the device resonant frequency. In addition, the asymptotic behaviour of the model can also be guaranteed by matching at extreme (low/high) frequency values. The FOAMM toolbox, based on finite-order hydrodynamic approximation by moment-matching, is a user-friendly platform allowing parametric system identification for either the radiation convolution term in (1), or the complete force-to-motion WEC dynamics in (5) (Pena-Sanchez et al., 2019). In this study, the FOAMM toolbox is used to identify a state-space model for the complete (force-to-motion) WEC dynamics.

6. Case study

The structure considered for this study is a point absorber-type WEC with the physical properties shown in Fig. 3. The buoy has an axisymmetric cylindrical geometry, with both radius and height of 0.25 m, and a hemispherical bottom with radius 0.25 m. The mass of the device is 43.67 kg, and the centre of the mass is located at a vertical distance of 0.191 m from the bottom-most point of the buoy. For CNWT simulation, the buoy is located at the centre of a 6 m deep tank with a water depth of 3 m as shown in Fig. 2. The tank spans a length of $L = 14$ m in the x- and y–directions, designed to be six wavelengths of the waves occurring at the peak frequency of the radiation damping of the WEC (4.56 rad/s), obtained from NEMOH (Babarit and Delhommeau, 2015). The NWT

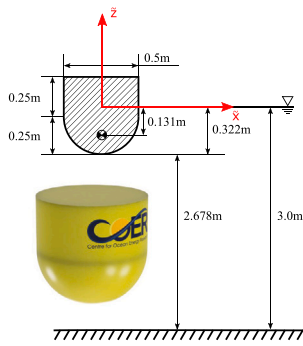[1] From now on, the notation [] refers to discrete samples.

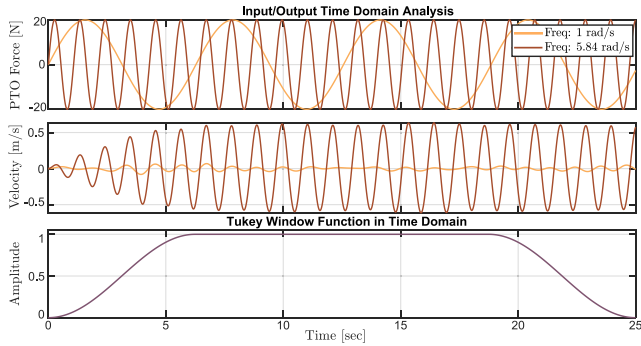**Fig. 3.** Schematic of the considered WEC structure.

Fig. 4. Time traces of the input/output signals in the CNWT for sinusoidal input signals with amplitude of 20 N and frequencies of 1 rad/s and 5.84 rad/s, along with Tukey ($\alpha = 0.5$) window profile.

setup is a modified version of that used in Farajvand et al. (2021), with further mesh refinement applied to ensure the fidelity of the NWT simulation. The smallest buoy displacement resulting from the input force is used to design the mesh sizes around the buoy, with a minimum cell dimension of 0.0054 m (3 cells per smallest displacement, induced by the smallest force amplitude at high frequency asymptote), giving a total number of NWT cells of 4.06 million. (For a screen shot of the spatial discretisation and computational mesh of the NWT, the interested reader is referred to Farajvand et al. (2022)).

The input excitation force is monochromatic sinusoidal, $f_u(t) = A\sin(\omega t)$, where A and ω are the amplitude and frequency of the sinusoids, respectively. Considering the limitations of the NWT dimensions, and the simulation duration, pure sinusoidal signals have been shown to provide high-fidelity representation of the system in terms of ETFE (for a detailed input signal synthesis to characterise dynamical uncertainty in WEC systems, the interested reader is referred to Farajvand et al. (2022)), which is a result of spending sufficient time at each frequency (low frequency variation ratio, i.e. high signal spectral permanency.) However, a relatively long experimentation time is required to cover the complete amplitude and frequency space. In this study, the sinusoidal excitation signals comprise a total of 96 individual experiments, combining the amplitude set $A_i = \{20, 40, 60, 80, 100, 120\}$ N with frequencies $\Omega_j \in \{0.2, 1, 2, 3, 4, 4.5, 5, 5.5, 6, 6.5, 7, 8, 9, 10, 18.89\}$ rad/s, plus a specific resonance frequency tailored to each amplitude set. This selection of frequencies and amplitudes gives a smooth representational transition between the ETFE points corresponding to discrete values of amplitude/frequency. The frequency range covers the complete dynamical range (with respect to the resonance frequency), and the amplitude range selection, ranging from linear behaviour (smallest amplitude) to amplitudes almost forcing the device out of the water (largest amplitude) and intermediate values, covers a full dynamical characterisation of the nonlinear system. Moreover, the amplitude set A_i perfectly covers the amplitudes corresponding to scaled (scaling
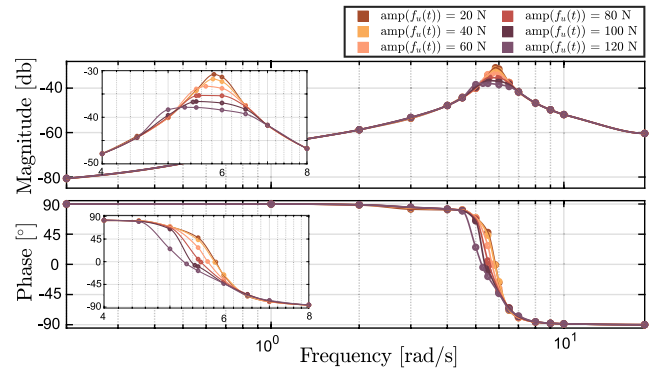

Fig. 5. ETFEs of the CNWT experiments using sinusoidal input signals with 6 amplitude levels.
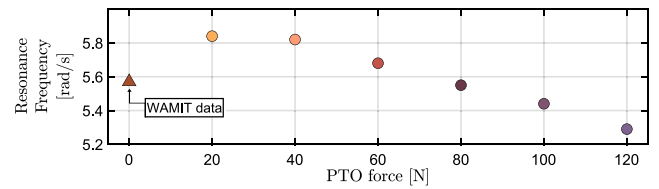

Fig. 6. Resonance frequency corresponding to different amplitude levels of input signals.

factor of 1/30th) operational conditions at the AMETS test site (Heller, 2011) with the maximum excitation force amplitude of 60N (Windt et al., 2021). Each experiment is driven by a finite set of N time-domain samples of input signals (exciting force signals) that generate a corresponding set of N output samples (which in this case are heave velocities). The NWT simulation interval of the sinusoidal experiments is [0, 25] s which guarantees enough spectral permanency time at each frequency and avoids wave reflections (Farajvand et al., 2021). By way of example, input/output time domain analysis for two sample experiments, with an amplitude of 20 N and frequencies of 1 rad/s and 5.84 rad/s (the resonance frequency of the system corresponding to a 20 N input amplitude force), is presented in Fig. 4. The transient response in the velocity time trace corresponding to a 20 N input signal, at 5.84 rad/s, is mitigated by the application of a Tukey window. Considering the longest transient response among the output time-domain signals from the 96 experiments, a Tukey window according to Eq. (13) with $\alpha = 0.5$ is applied, also shown in Fig. 4. Each series of experiments generates a single frequency point in the ETFE (Eq. (11)) of the system, obtained from the calculation of the DTFT of the output signal $v(t)$ and the known amplitude and phase of the sinusoidal input signal ($f_u(t)$). ETFEs, covering the complete amplitude range A_i, and their corresponding frequency ranges, with further ETFE refinement (based on the physical principles articulated in Section 2.1) are obtained based on: (A) ETFE phase components are corrected to 90° and −90° at the low and high-frequency asymptotes, respectively, and (B) The system phase is forced within ±90° degrees *for all frequencies*, respecting the passive nature of the system.

The ETFEs, and their interpolation across frequency points using piecewise cubic Hermite interpolating polynomials (PCHIPs), are shown in Fig. 5.

Due to nonlinearity, different levels of input signal amplitude result in different ETFEs. One major characteristic observed from the determined ETFEs is an increasing trend of the bandwidth, and a decreasing trend of the peak frequency response (resonance frequency), as the amplitude of the input signal increases. It can be concluded that, as the amplitude of the input force gets larger, the resonance frequency decreases, and the damping ratio increases. The resonance frequency, corresponding to each amplitude level (from CNWT data),

is presented in Fig. 6, showing a decreasing resonance frequency trend with increasing input signal amplitude. The results of the resonance frequencies from force-input experiments are also compared with the resonance frequency from WAMIT data (effectively zero input amplitude) in Fig. 6. Note that the resonance frequency obtained from WAMIT (infinitesimally small amplitude) data violates the expected resonance frequency trend, suggesting that a WAMIT model may not provide a representative model of the system, even at relatively low excitation amplitudes. (However, due to extreme computational effort and higher mesh resolution requirement, the convergence towards the 0 N point is not resolved beyond the $amp(f_u(t)) = 20$ N point.)

6.1. System identification results

State-space representations of the WEC system, at different force levels, are obtained using the FOAMM (Faedo et al., 2018) toolbox, where three 'cardinal' points of each ETFE, i.e., low-frequency asymptote, resonance frequency, and high-frequency asymptote, are selected manually as inputs to the FOAMM toolbox. The order of the output system will be twice the number of selected frequencies (6th order in this case) with exact frequency matching based on the selection of the desired set of frequencies (e.g. the resonance frequency) in the manual mode. By way of example, the state, input, and output matrices of the state-space model according to Eq. (7), obtained for an 80 N input level, are:

$$A = \begin{bmatrix} -692.92 & 693.12 & -692.92 & 692.92 & -692.92 & 692.92 \\ -640.69 & 640.49 & -640.49 & 640.49 & -640.49 & 640.49 \\ -0.51 & 0.51 & -0.51 & 6.01 & -0.51 & 0.51 \\ -7.05 & 7.05 & -12.55 & 7.05 & -7.05 & 7.05 \\ -19.00 & 19.00 & -19.00 & 19.00 & -19.0 & 37.89 \\ -13.96 & 13.96 & -13.96 & 13.96 & -32.85 & 13.96 \end{bmatrix},$$

$$B = \begin{bmatrix} 692.92 & 640.49 & 0.51 & 7.05 & 19.00 & 13.96 \end{bmatrix}^\top,$$

$$C = \begin{bmatrix} 0.00 & 0.00 & 0.01 & -0.01 & 0.00 & 0.00 \end{bmatrix},$$

respectively, with corresponding pole pairs:

Pole pairs of the 6th order system
$-0.51 \pm 5.50i$
$-12.46 \pm 12.21i$
$-12.48 \pm 12.36i$

The frequency response of the obtained parametric model using the FOAMM toolbox (solid-red), (which will be used to perform the dominant dynamical assessment), along with the target frequency response (dashed-blue), and the interpolated frequencies (green-dots), for all the input amplitude forces, are shown in Fig. 7. The identified system fits well with the actual system, for low input amplitudes, and the error between actual and identified models, calculated in terms of the Mean Absolute Percentage Error (MAPE), gets larger as the input amplitude increases, recognising the increasing difficulty of fitting a linear model for greater input amplitudes. The same identification procedure is applied to a WEC model obtained from WAMIT (zero-input signal) in order to compare the results. The MAPE between actual and identified models, corresponding to each input amplitude level, is presented in Table 1. Note that the MAPE value, corresponding to each input amplitude level, depends on the manual selection of the desired (matching) frequency points chosen in the FOAMM toolbox.

6.2. Dominant pole analysis

The identified systems in Section 6.2 are used to locate the least damped (slowest) poles, which most affect the behaviour of the dynamic system. For a stable linear system, the relative dominance of the poles is determined by the ratio of the real parts of the poles nearest the $j\omega$ axis, where the suggested value is 3–5 in Wang et al. (2008) and Nedić et al. (2017), and 10 in Dorf and Bishop (2008). As the

Table 1
The MAPE between actual and identified 6th order models corresponding to each input amplitude level.

Input signal amplitude [N]	MAPE
0 (WAMIT)	0.000895
20	0.029779
40	0.027002
60	0.075799
80	0.115651
100	0.155575
120	0.164085

requirement that a ratio >3 may not be fulfilled, the ratio of the real parts of the poles >5 is assigned where the pole (or complex pair) with the smallest real part, i.e. closest to the imaginary axis, is the dominant pole (or complex pair), and other poles may be regarded as relatively insignificant. A pole dominancy condition for each input amplitude level (including three pairs of complex conjugate poles for each of the 6th order identified models) is considered. Pole dominance, for the models corresponding to each input amplitude level, is calculated by the ratio of the real parts of the two pole pairs closest to the imaginary axis, with results listed in Table 2. For the models obtained with input force amplitudes of 20 N, 40 N, 60 N, and 120 N the closest pole pairs to the imaginary axis cannot be truly considered as dominant poles, but the pole dominancy condition is satisfied for the models corresponding to 0 N (the WAMIT model), 80 N and 100 N input amplitudes. There is no clear trend of pole dominance with respect to the input signal amplitude, which can be possibly due to the obtained identification error, computed in terms of MAPE, between the target and identified frequency responses. In particular, for some cases, the identification error is larger in the region around resonance while, for other cases (higher input forces), the error is more significant at the extremes of the frequency range, considered for error computation, as represented in Fig. 7.

Poles closer to the imaginary axis represent slower modes, indicating a lower damping effect. The least damped pole pairs (closest pole to the imaginary axis), corresponding to the identified models of all input amplitude levels, along with the dominant pole pair obtained from the WAMIT model, are presented in Fig. 8. Since the magnitude of the real part of the least damped poles of the models show an increase as the input amplitude force increases, it can be concluded that larger input amplitudes correspond to stronger damping (possibly due to viscous effects). Note that a linearised viscous damping effect can be approximated using Lorentz linearisation (Terra et al., 2005).

Note that the least damped pole locations, corresponding to the smallest input amplitude force (close to a truly linear model), is very similar to the dominant pole of the WAMIT model, indicating the relative accuracy of the WAMIT model for representing the WEC model excited with very small input amplitude forces. However, the WAMIT model fails to provide a representative model of the system dynamics when the device is subject to high input amplitude forces, typical of a WEC in power production mode. However, the convergence of the CFD-derived pole locations on the WAMIT poles, for small input amplitude provides a degree of validation of the modelling method, and is similar to results obtained for free-response tests (Davidson et al., 2015).

In Fig. 8, a gentle trend in the values of the imaginary components of the least damped poles can be observed, essentially related to the oscillatory frequency in the response. The trend of the imaginary component of the least damped poles is similar to the resonance frequency trend presented in Fig. 6, i.e. the imaginary component of the least damped poles decreases as the input amplitude increases, and a discrepancy of the trend is observed with the zero-input data, obtained from the WAMIT model. In a 2nd order system, the imaginary component of the pole corresponds to the value of $\omega_n \sqrt{1 - \zeta^2}$ (the damped 'natural' frequency), where ω_n is the natural frequency of the device, related to the resonance frequency of the system ($\omega_n \sqrt{1 - 2\zeta^2}$) (depicted in
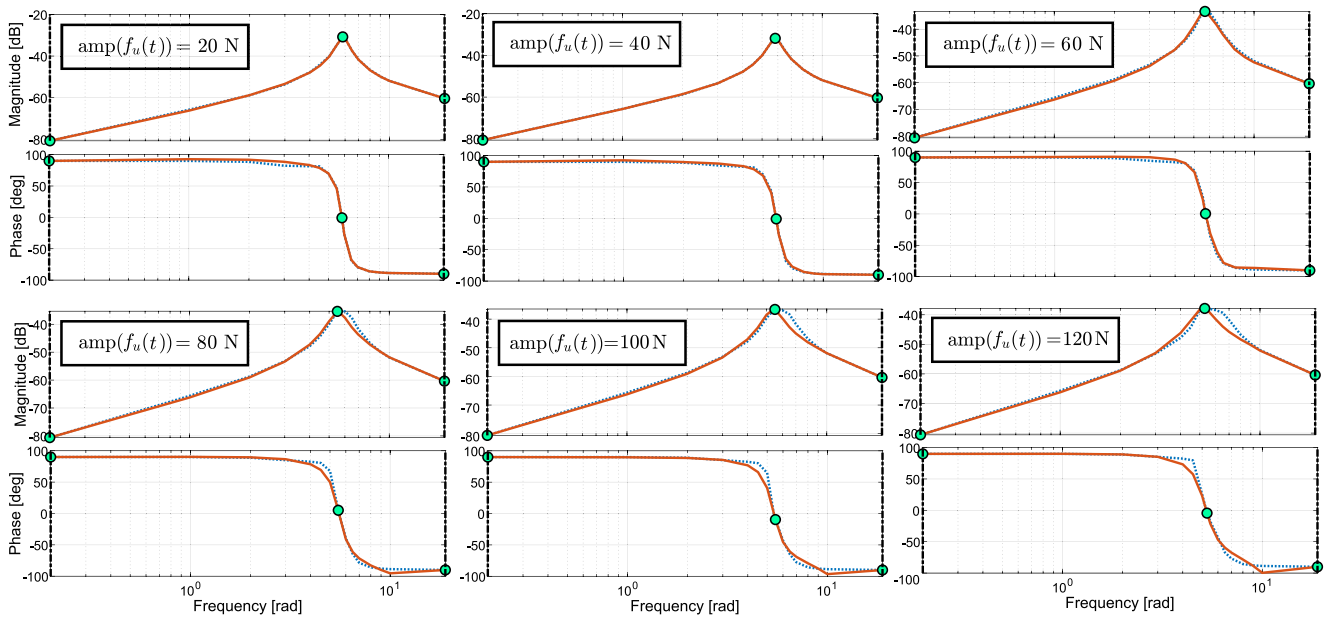
Fig. 7. The frequency response of the obtained parametric model using FOAMM toolbox (solid-red), along with the target frequency response (dashed-blue), and the interpolated frequencies (green-dots) for all the input amplitude forces.
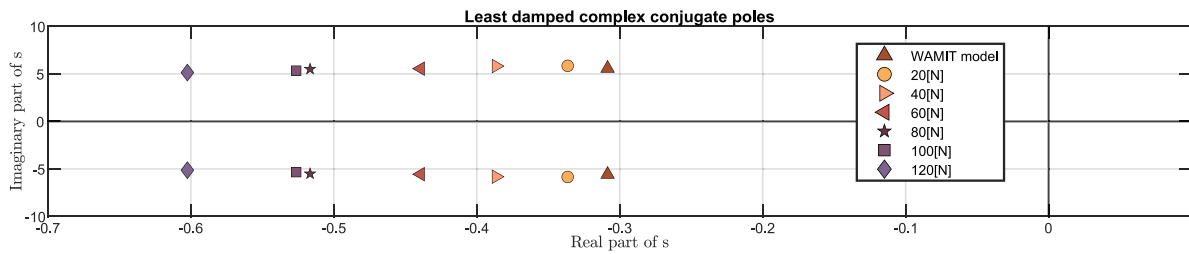

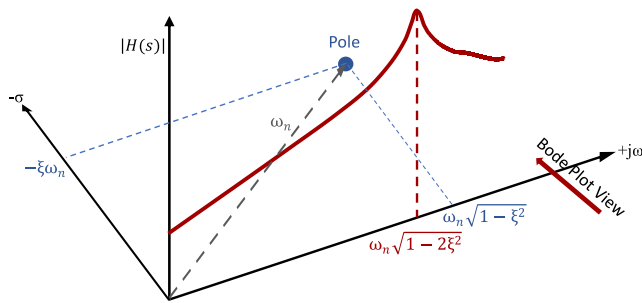**Fig. 8.** Location in the complex-plane of the least damped model poles.

Fig. 9. 3D view of pole diagram and Bode plot.

Table 2
Pole dominance assessment for system models corresponding to different input amplitude levels.

Force amplitude [N]	Ratio of the real parts of the poles	Pole dominance
0 (WAMIT)	12.56	✓
20	3.92	✗
40	4.51	✗
60	2.04	✗
80	24.12	✓
100	5.07	✓
120	4.46	✗

Table 3
Imaginary components of the dominant poles corresponding to input signal amplitudes.

Input signal amplitude [N]	Imaginary part of the least damped poles
0 (WAMIT)	5.580
20	5.845
40	5.819
60	5.554
80	5.508
100	5.343
120	5.136

Fig. 9 in three-dimensions), and ζ is the damping factor. In this study, there is no clear relationship between the imaginary components of the least damped poles and the resonance frequencies obtained from ETFEs (Fig. 6). A possible explanation related to the error of approximating the system model using the FOAMM toolbox, and the fact that the least damped poles are not truly dominant poles for all models. Imaginary component values, for the least damped poles corresponding to input signal amplitudes, are presented in Table 3.

One particularly significant result obtained in this study is the similarity of the trend of the least damped poles location of the force-input CNWT experiments and WAMIT model (Fig. 8) to the dominant poles location trend obtained from free-decay CNWT experiments and a

BEM presented in Davidson et al. (2015) (Fig. 14). This provides some level of cross validation, though both sets of results are obtained using different stimuli (forced input Vs non-zero initial condition).

7. Conclusion

In this study, representative linearised WEC models are investigated by performing system identification using force input (PTO force) CNWT experiments. Considering the true complexity of real WEC models (viz the NS equations), force-input experiments, with careful design of input signals to cover the full range of frequencies and amplitudes likely to be encountered during system operation, are capable of providing a sufficiently *representative linear* model set that can be used for dynamical assessment of WECs, and for model-based control design, using either a single representative model, or some form of gain scheduling (Leith and Leithead, 2000), interpolating between models/controllers. The following conclusions can be drawn regarding the dominant dynamical assessment of the WEC system:

- Analysis of the resonance frequency of the system, from the ETFE results of the input-force CNWT experiments and WAMIT data, shows an increasing trend in resonance frequency as the amplitude of the input force decreases, with a small deviation in the trend due to a less representative model obtained from WAMIT data.
- Investigation of the least damped poles of the system sheds light on two important dynamical behavioural aspects of the system: *(A)* The real part of the least damped poles gets closer to the imaginary axis, indicating a lower damping effect, as the amplitude of the input-force decreases, and *(B)* The imaginary part of the least damped poles is related to the resonance frequency, and thus shows the same trend as the resonance frequency.
- The trend obtained from the force-input CNWT experiments (and WAMIT model), for the real part of the least damped poles of the system, is very similar to the results obtained from the free-decay CNWT experiments (and BEM model) reported in Davidson et al. (2015).

Finally, a dominant 2nd order WEC model has been shown to have utility in the design of relatively simple controllers for WECs (Fusco and Ringwood, 2011), while variations in real parts of poles can be traced to implications for sensitivity and robustness (Ringwood et al., 2019).

CRediT authorship contribution statement

Mahdiyeh Farajvand: Conceptualization, Methodology, Investigation, Formal analysis, Software, Writing – original draft, Writing – review & editing, Visualization. **Demián García-Violini:** Methodology, Formal analysis, Software, Writing – review & editing. **John V. Ringwood:** Conceptualization, Writing – review & editing, Supervision, Funding acquisition, Project administration.

Declaration of competing interest

The authors declare that they have no known competing financial interests or personal relationships that could have appeared to influence the work reported in this paper.

Data availability

No data was used for the research described in the article.

Acknowledgements

References

Armesto, J.A., Guanche, R., Iturrioz, A., Vidal, C., Losada, I.J., 2014. Identification of state-space coefficients for oscillating water columns using temporal series. Ocean Eng. 79, 43–49.

Babarit, A., Delhommeau, G., 2015. Theoretical and numerical aspects of the open source BEM solver NEMOH. In: 11th European Wave and Tidal Energy Conference, Nantes, France (EWTEC2015).

Babarit, A.l., Mouslim, H., Cle´ment, A., Laporte-Weywada, P., 2009. On the numerical modelling of the non linear behaviour of a wave energy converter. In: International Conference on Offshore Mechanics and Arctic Engineering, Vol. 43444. pp. 1045–1053.

Bacelli, G., Coe, R.G., Patterson, D., Wilson, D., 2017. System identification of a heaving point absorber: Design of experiment and device modeling. Energies 10 (4), 472.

Cummins, W.E., 1962. The impulse response function and ship motions. Schiffstechnik 47, 101–109.

Davidson, J., Giorgi, S., Ringwood, J.V., 2015. Linear parametric hydrodynamic models for ocean wave energy converters identified from numerical wave tank experiments. Ocean Eng. 103, 31–39.

Dorf, R.C., Bishop, R.H., 2008. Modern Control Systems. Pearson Prentice Hall.

Faedo, N., Peña-Sanchez, Y., Ringwood, J.V., 2018. Finite-order hydrodynamic model determination for wave energy applications using moment-matching. Ocean Eng. 163, 251–263.

Falnes, J., 2002. Ocean Waves and Oscillating Systems: Linear Interactions Including Wave-Energy Extraction. Cambridge Univ. Press.

Farajvand, M., García-Violini, D., Windt, C., Grazioso, V., Ringwood, J., 2021. Quantifying hydrodynamic model uncertainty for robust control of wave energy devices. In: 14th European Wave and Tidal Energy Conference (EWTEC), Plymouth. pp. 2251–1:2251–10.

Farajvand, M., Grazioso, V., García-Violini, D., Ringwood, J.V., 2022. Uncertainty estimation in wave energy systems with applications in robust energy maximising control. Renew. Energy 203, 194–204.

Fusco, F., Ringwood, J.V., 2011. Suboptimal causal reactive control of wave energy converters using a second order system model. In: The 21st Intl. Offshore and Polar Eng. Conf., Hawaii. ISOPE.

García-Violini, D., Farajvand, M., Windt, C., Grazioso, V., Ringwood, J.V., 2021. Passivity considerations in robust spectral-based controllers for wave energy converters. In: 2021 XIX Workshop on Information Processing and Control (RPIC), San Juan, Argentina. IEEE, pp. 1–6.

García-Violini, D., Peña-Sanchez, Y., Faedo, N., Ringwood, J.V., 2020. An energy-maximising linear time invariant controller (LiTe-Con) for wave energy devices. IEEE Trans. Sustain. Energy 11 (4), 2713–2721.

Heller, V., 2011. Scale effects in physical hydraulic engineering models. J. Hydraul. Res. 49 (3), 293–306.

Khalil, H.K., 2014. Nonlinear Control. Pearson Higher Ed.

Leith, D.J., Leithead, W.E., 2000. Survey of gain-scheduling analysis and design. Int. J. Control 73 (11), 1001–1025.

Letournel, L., Ferrant, P., Babarit, A., Ducrozet, G., Harris, J.C., Benoit, M., Dombre, E., 2014. Comparison of fully nonlinear and weakly nonlinear potential flow solvers for the study of wave energy converters undergoing large amplitude motions. In: International Conference on Offshore Mechanics and Arctic Engineering, Vol. 45547. American Society of Mechanical Engineers, V09BT09A002.

Ljung, L., 2010. Perspectives on system identification. Annu. Rev. Control 34 (1), 1–12.

Merigaud, A., Gilloteaux, J.-C., Ringwood, J.V., 2012. A nonlinear extension for linear boundary element methods in wave energy device modelling. In: International Conference on Offshore Mechanics and Arctic Engineering, Vol. 44915. American Society of Mechanical Engineers, pp. 615–621.

Nedić, N.N., Prodanović, S.L., Dubonjić, L.M., 2017. Decoupling control of tito system supported by dominant pole placement method. Facta Univ. Ser.: Mech. Eng. 15 (2), 245–256.

Ogilvie, T.F., 1964. Recent progress toward the understanding and prediction of ship motions. In: 5th Symp. on Naval Hydr., Vol. 1. Bergen, pp. 2–5.

Pena-Sanchez, Y., Faedo, N., Penalba, M., Giuseppe, G., Mérigaud, A., Windt, C., Violini, D.G., LiGuo, W., Ringwood, J., 2019. Finite-Order hydrodynamic Approximation by Moment-Matching (FOAMM) toolbox for wave energy applications. In: European Wave and Tidal Energy Conference Proceedings (EWTEC),Naples. pp. 1448–1:1448–9.

Penalba, M., Giorgi, G., Ringwood, J.V., 2017. Mathematical modelling of wave energy converters: A review of nonlinear approaches. Renew. Sustain. Energy Rev. 78, 1188–1207.

Pérez, T., Fossen, T., 2008. Time-vs. frequency-domain identification of parametric radiation force models for marine structures at zero speed. Model. Identif. Control 29 (1), 1–19.

Perez, T., Fossen, T.I., 2011. Practical aspects of frequency-domain identification of dynamic models of marine structures from hydrodynamic data. Ocean Eng. 38 (2–3), 426–435.

Prabhu, K.M., 2014. Window Functions and their Applications in Signal Processing. Taylor & Francis.

Ringwood, J.V., Mérigaud, A., Faedo, N., Fusco, F., 2019. An analytical and numerical sensitivity and robustness analysis of wave energy control systems. IEEE Trans. Control Syst. Technol. 28 (4), 1337–1348.

Terra, G.M., van de Berg, W.J., Maas, L.R., 2005. Experimental verification of Lorentz'linearization procedure for quadratic friction. Fluid Dyn. Res. 36 (3), 175.

Wamit Inc, 2022. WAMIT User Manual. http://tinyw.in/7u4T. (Accessed online: 2022-04-11).

Wang, Q.-G., Zhang, Z., Astrom, K.J., Zhang, Y., Zhang, Y., 2008. Guaranteed dominant pole placement with PID controllers. IFAC Proc. Vol. 41 (2), 5842–5845.

Windt, C., Davidson, J., Ransley, E.J., Greaves, D., Jakobsen, M., Kramer, M., Ringwood, J.V., 2020. Validation of a CFD-based numerical wave tank model for the power production assessment of the wavestar ocean wave energy converter. Renew. Energy 146, 2499–2516.

Windt, C., Davidson, J., Ringwood, J.V., 2018. High-fidelity numerical modelling of ocean wave energy systems: A review of computational fluid dynamics-based numerical wave tanks. Renew. Sustain. Energy Rev. 93, 610–630.

Windt, C., Davidson, J., Schmitt, P., Ringwood, J.V., 2019. On the assessment of numerical wave makers in CFD simulations. J. Mar. Sci. Eng. 7 (2), 47.

Windt, C., Faedo, N., Penalba, M., Dias, F., Ringwood, J.V., 2021. Reactive control of wave energy devices–the modelling paradox. Appl. Ocean Res. 109, 102574.